Article

Engineering Photoresponse in Epitaxial BiFe$_{0.5}$Cr$_{0.5}$O$_3$ Thin Films through Structural Distortion

Mohammad Moein Seyfouri, Dawei Zhang, César Menéndez, Daniel Sando, Qi Zhang, Claudio Cazorla, Jan Seidel, and Danyang Wang*

Read Online

ACCESS | 📊 Metrics & More | 📄 Article Recommendations | 🆂🆈 Supporting Information

ABSTRACT: Multiferroic BiFe$_{0.5}$Cr$_{0.5}$O$_3$ (BFCO) thin films are promising candidates for emerging optoelectronics and all-oxide solar absorbers. Yet, a thorough understanding of the structural evolution and associated changes in the functional properties of BFCO is lacking. Here, we explore thickness-dependent structural phase transitions in the epitaxial BFCO films and ascertain the impact of the accompanying crystallographic distortions on their photoresponse. The results show that the strain imposed by the substrate changes the crystal symmetry, inducing a transition from a tetragonal-like phase to a rhombohedral-like phase through a rather complex strain relaxation mechanism upon increasing film thickness. This change in crystallographic distortion also induces a shift of ∼150 meV in the bandgap. Moreover, wavelength-resolved photocurrent measurements reveal that the absorption onset is red-shifted for the tetragonal-like structure, implying light absorption up to wavelengths of 800 nm. First-principles calculations shed further light on the symmetry-induced changes in the electronic structure of the BFCO films. The crystallographic symmetry is shown to be a decisive factor in modifying the valence band maximum and conduction band minimum characteristics in the perovskite oxides, revealing an emerging type of Mott multiferroic in the BFCO system. This work provides a practical strategy to further engineer the optoelectronic properties of the multiferroic oxide films through thickness-induced phase transitions.
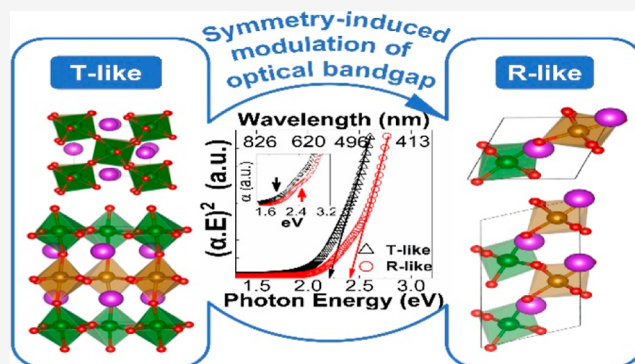
1. INTRODUCTION

Over the past decades, the increasing quest for miniaturization of devices has resulted in the conceptualization of unexplored research areas aiming to couple different functionalities in the emerging thin-film technologies. Not surprisingly, ferroelectric oxide perovskites—exhibiting a switchable spontaneous polarization—have been the subject of myriad studies to pair their functional features, including (but not limited to) ferroic order and optical response.[1,2] In conventional semiconductors, the separation of photoexcited electrons and holes relies on the built-in electric field created at the p−n junction[3] and p−i−n heterojunction configuration.[4] However, this approach presents some limitations, including the short extent of the built-in electric field and the necessary introduction of the dopant species.[5] Alternative routes have been proposed to efficiently separate photoexcited carriers in semiconductors. A promising avenue is to exploit the intrinsic electric field and electric polarization in ferroelectric materials to induce the electron−hole pair dissociation[6] and achieve above-bandgap photovoltages and switchable photocurrents.[7] Ferroelectric materials, therefore, have emerged as very promising candidates to revolutionize the field of optoelectronic devices.[8] Nevertheless, a long-standing problem in ferroelectric photo-

voltaics is the low photocurrent output originating from their wide bandgap and reduced charge mobility as compared to conventional semiconductors.[9] To the best of our knowledge, only a few narrow bandgap ferroelectric oxides have been reported that can absorb light in the visible wavelength, such as [KNbO$_3$]$_{1−x}$[BaNi$_{1/2}$Nb$_{1/2}$O$_{3−δ}$]$_x$,[10] BiFe$_{0.5}$Cr$_{0.5}$O$_3$ (BFCO),[11] Bi$_{3.25}$La$_{0.75}$Co$_1$Ti$_2$O$_{11.5}$,[12] and BiMnO$_3$.[13] In particular, the BFCO perovskite exhibited bandgap tunability relying on Fe/Cr cation ordering, thus allowing the highest power conversion efficiency (8.1%) realized in a multilayered oxide perovskite.[14]

Experimental studies have shown that BFCO in both epitaxial thin-film and bulk ceramic forms is isostructural to BiFeO$_3$ (BFO), having a rhombohedrally distorted structure.[15,16] From the electronic structure viewpoint, the conduction band edge of the rhombohedral perovskite is positioned at higher energies due to the antibonding TM-O
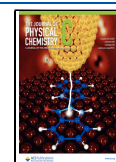
orbital interaction in the A-point of the Brillouin zone.[17] Thus, further tuning of the perovskite bandgap appears to be possible through crafting different crystal symmetries. Indeed, the perovskite unit cell can be distorted through hydrostatic pressure or elastic strain,[18] leading to cationic displacements and/or deformation of the oxygen octahedra, both of which can influence the material properties distinctly.

In this work, we explore thickness-induced structural phase transitions in the BFCO thin films grown on $SrRuO_3$ (SRO)-buffered (001) $SrTiO_3$ substrates. Structural characterization reveals that the substrate-imposed strain can change the symmetry of the film, which transitions from a tetragonal-like (T-like) phase to a rhombohedral-like (R-like) phase as the film thickness increases. Spectroscopic ellipsometry results combined with density functional theory (DFT) show that the bandgap notably changes through the structural phase transition. Photoresponse measurements using wavelength-resolved conductive atomic force microscopy (c-AFM) demonstrate that the onset of optical absorption is also red-shifted in the T-like BFCO film. These results reveal that within the BFCO system, other tuning knobs, including strain and film symmetry, can be used to tailor the functional optical response.

2. METHODS

Pure phase BFCO thin films were prepared on (001) single-crystal $SrTiO_3$ substrates (Shinkosha Co Ltd, Japan) by laser molecular beam epitaxy (Pascal Co Ltd, Japan). All films were grown through ablation of an in-house-sintered ceramic target with a KrF excimer laser (248 nm wavelength). Excess Bi_2O_3 (20 wt %) was used to compensate for highly volatile bismuth during the film deposition and target preparation. The laser fluence was kept constant at about 2 J cm^{-2}, while the BFCO films were deposited at a substrate temperature of 620 °C under a dynamic oxygen pressure of 4 mTorr. To perform SPM measurements, the $SrRuO_3$ bottom electrode was deposited in situ on the substrate at 680 °C under 100 mTorr of oxygen before growing the BFCO layer.

X-ray diffraction (XRD) was conducted using a MRD PANAlytical X-ray diffractometer and a Rigaku SmartLab with a Cu Kα source. Reciprocal space mapping (RSM) was utilized to investigate the lattice structure of BFCO films. X-ray reflectivity (XRR) was used to determine the layer thickness by fitting the data in X'Pert reflectivity software (PANAlytical B.V., the Netherlands).

The surface morphology of BFCO films was inspected using a commercial atomic force microscope (Bruker Dimension Icon). X-ray photoemission spectroscopy (XPS) was recorded on a ESCALAB250Xi (Thermo Scientific) utilizing a monochromatic Al Kα source (160 W) at a base pressure lower than 1×10^{-9} Torr. The spectra were adjusted with respect to the adventitious hydrocarbon (C 1s = 284.8 eV).

The optical properties of the BFCO films were characterized using a variable-angle spectroscopic ellipsometer (J.A. Woollam M-2000 DI) at room temperature. Data were recorded in the 200−1000 nm wavelength range at three angles of incidence (55, 65, and 75°) (see the Supporting Information). The optical dispersion function of the films was described by an optical model composed of the substrate, thin film, and layer of surface roughness on top expressed by the Bruggeman effective medium approximation. Parameterization of the optical constant includes multiple Gaussian oscillators with central energies associated with the charge−transfer

transition. The optical bandgap was estimated using Tauc's extrapolation method from $(\alpha \cdot E)^2$ versus photon energy plot,[19] where the absorption coefficient was derived from the formula $\alpha = 4\pi k/\lambda$.

Scanning probe microscopy measurements, which include piezoresponse force microscopy (PFM), Kelvin probe force microscopy (KPFM), and c-AFM, were performed using a commercial atomic force microscopy system (AIST-NT Smart SPM 1000) under an ambient atmosphere. Conductive platinum-coated tips (Mikromasch HQ: NSC35/Pt) with a force constant of ~5 N/m and a tip radius less than 30 nm were used for the imaging mode. An external tunable illumination source (FemtoPower 1060) was used to illuminate the samples at an angle of 30° to avoid shadowing from the probe tip. Detailed laser intensity as a function of wavelength can be found in the Supporting Information. The laser on/off experiment was first conducted in a dark environment for half of the imaging size and then conducted with laser on for the half of the remaining image, which allows a direct comparison of the property measured in the dark and under illumination.

First-principles spin-polarized calculations based on DFT were performed with the generalized gradient approximation proposed by Perdew, Burke, and Ernzerhof (PBE) as implemented in the VASP package.[20] We employed the Hubbard-U scheme derived by Dudarev et al. to deal with the 3d electrons in Cr and Fe ions (3.7 and 5.0 eV, respectively).[21] We used the projected augmented wave method with the following ions (and valence electrons): Cr ($3s^23p^64s^13d^5$), Fe ($3p^64s^13d^7$), Bi ($6s^25d^{10}6p^3$), and O ($2s^22p^4$).[22] A Γ-centered $4 \times 6 \times 6$ k-point grid and an energy cut-off of 800 eV were employed. All geometry relaxations were performed on a $2 \times \sqrt{2} \times \sqrt{2}$ supercell containing 20 atoms (4 formula units), and the forces on the atoms were all relaxed below 0.01 eV/Å. All possible Fe/Cr ionic positions and spin magnetic arrangements (i.e., ferromagnetic and antiferromagnetic type A, G, and C) compatible with our simulation supercell were explored; the results presented in the next sections correspond to those configurations rendering the lowest energies. The vibrational stability of each phase was checked through the calculation of phonons at the high-symmetry reciprocal space Γ points. We estimated the ferroelectric polarization of BFCO films with the Born effective charges method[23] and used the HSE06 hybrid functional to compute their electronic density of states and bandgap energies.[24]

3. RESULTS AND DISCUSSION

3.1. Structural Evolution. This paper focuses on three epitaxial BFCO films with nominal thicknesses of 30, 70, and 130 nm. AFM images for the films reveal a corrugated surface with an island-like morphology consistent with a 3D film growth mode (Figure S2). The surface showed an increase in the roughness from 1.65 to 2 nm with increasing film thickness. Notably, these roughness values are lower than those previously reported for BFCO films of similar thickness.[11]

XRD was used to inspect the crystal structure of the films. Coupled $\theta-2\theta$ scans demonstrate that all the BFCO heterostructures are grown with the out-of-plane (OP) direction oriented parallel to the (00l) plane of the substrate (Figure 1a,b). No secondary phases were detected within the resolution limit of the XRD measurement. As presented in Figure 1d, the Laue fringes, albeit less pronounced around the
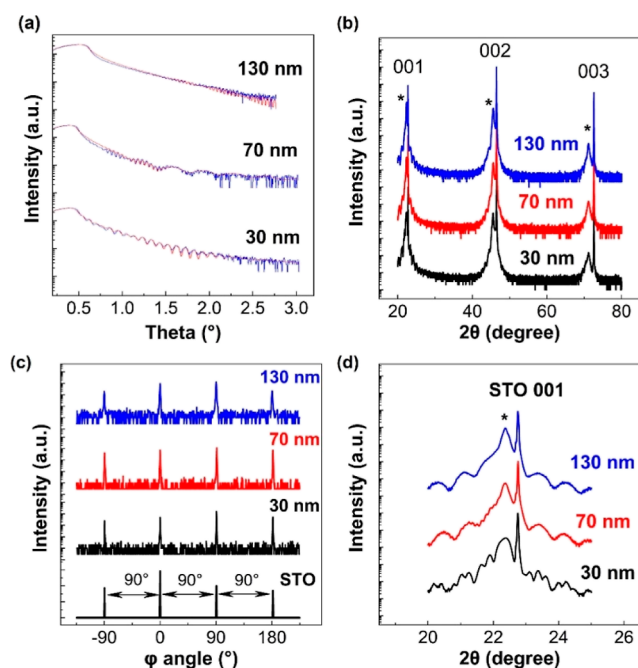
Figure 1. (a) XRR pattern (the red line represents the fitted pattern). (b) Coupled $\theta-2\theta$ scan of the three samples. The asterisks identify the BFCO peaks. (c) Phi scan recorded around the 101 peak, highlighting the epitaxial growth of the BFCO film on the substrate. (d) Zoom around 001 reflection.

higher orders, attest to smooth interfaces and high coherency of the film layers.[25] To obtain information about the layer thicknesses and quality of the interfaces, XRR measurements and fitting analyses were carried out (see Table S1). Next, the cube-on-cube epitaxy was confirmed by performing XRD phi scans of the (101) BFCO films, which show four peaks separated by 90° at the same angle as the substrate (Figure 1c). In addition, the narrow, i.e. smaller than 0.3°, full width at half-maximum (FWHM) of the rocking curve around 002 reflection confirms the high crystalline quality of all the three samples (Figure S3). Note that the thicker films exhibited larger FWMH—by a factor of 2—compared to the 30 nm-thick sample, which is associated with the larger mosaicity of the film.[26]

Intriguingly, the 001 diffraction peaks for the thinnest and thickest films reveal that the position of the film peak is comparable, implying that the lattice constant of epitaxial films along the c-axis remains unchanged regardless of the thickness (see Figure 1d). This is in stark contrast to the fact that for an in-plane compressively strained film, the OP lattice expansion is typically deemed to decrease with the thickness.[27] Nevertheless, a similar behavior is also observed in the strained BFO films, which exhibited a constant lattice parameter when the film thickness is below 90 nm, a rather confusing result.[28] Given these peculiarities, it is crucial to unfold the strain-relieving mechanism as the thickness increases.

The first step is to find the thickness beyond which the strain relaxation takes place. For the pseudomorphic epitaxy, the modified Matthews−Blakeslee (MB) model can predict the critical thickness for thin films where strain relaxation occurs by the misfit dislocation (details given in Supporting Information Section 4).[29] In our case, the critical thickness is estimated to be about 6 nm, above which the formation of the misfit dislocation becomes energetically favorable, and strain

relaxation initiates through the presence of dislocation. Note that the growth kinetics can considerably extend this range; however, the thickness of the epitaxial film needs to be constrained to just a few factors larger than the MB critical thickness to achieve a perfectly commensurate film with the minimum dislocation density.[30] Since the thinnest film in this study is at least 5 times beyond the MB critical thickness, it is not unreasonable to expect the presence of misfit dislocations.

Furthermore, it has been reported that the lattice parameters are more altered in the vicinity of dislocation,[31] resulting in an inhomogeneous strain distribution. In particular, this non-uniformity makes the thickness-dependent studies of perovskite thin films a grueling task.[30] Hence, to quantitatively investigate the inhomogeneous strain, we analyzed the diffraction line broadening as a function of the film thickness, using the Williamson−Hall relation (details given in Supporting Information Section 5).[32]

Remarkably, we observed that the inhomogeneous strain for the 30 nm thin film exceeds that of the thicker films. Note that the density of dislocation is rapidly increasing in the proximity of the critical thickness (~6 nm) before it saturates, leading to a higher inhomogeneous strain resulting from the dispersion of lattice parameters in a substantial fraction of the film thickness.[33] Therefore, we presume that the strain relaxation mechanism is not solely due to the formation of misfit dislocation.

To obtain a complete picture of strain relieving as a function of the film thickness, we have investigated the crystallographic evolution using RSM. Figure 2 presents the contour plots of the RSMs around the (003), (203), and (113) planes for the (00l)-oriented films with different thicknesses. The coincidence of the horizontal line in the symmetric (003) scan further confirms the earlier observation regarding the unchanged OP lattice parameter for the film thickness range in this study. However, Figure 2b,e,h show that the asymmetric 203 diffraction peak develops from a unique spot for the 30 nm-thick film, although it spreads out in the OP direction due to the finite thickness, to the separated peaks for 70 and 130 nm films. This observation clearly indicates that multiple crystallographic domains are developed as the film thickness increases.[34] Note that the twofold asymmetric reflections are slanted away from the q_z ($\parallel$ [001]) of the (003) spot, implying that these films have adopted a monoclinically distorted structure while the 30 nm-thick film has a T-like symmetry. The disappearance of the splitting pattern for the 30 nm-thick film suggests a tetragonal symmetry, showing that the films is fully clamped by the substrate with equal in-plane lattice constants resembling that of STO without structural twinning. Moreover, the formation of a single domain monoclinic structure in the 30 nm-thick film can be disregarded, as confirmed by further RSM studies in Figure S7.

Figure 3 highlights the variation of lattice parameters as a function of thickness where several salient features are observed (more details given in Supporting Information Section 6). First, the OP parameter (c_m) is almost constant (as mentioned earlier). Next, the average in-plane lattice parameter increases with the thickness, yet not exceeding the pseudocubic bulk value of 3.937 Å.[35] This confirms the residual strain in the unit cell due to the clamping effect of the substrate. Moreover, the (003) RSM plots recorded with the X-ray beam along the [110] directions reveal different patterns. It shows an apparent splitting along the [110] direction ($\phi = 45°$) for the 130 nm thin film, which implies titling of the (00l)
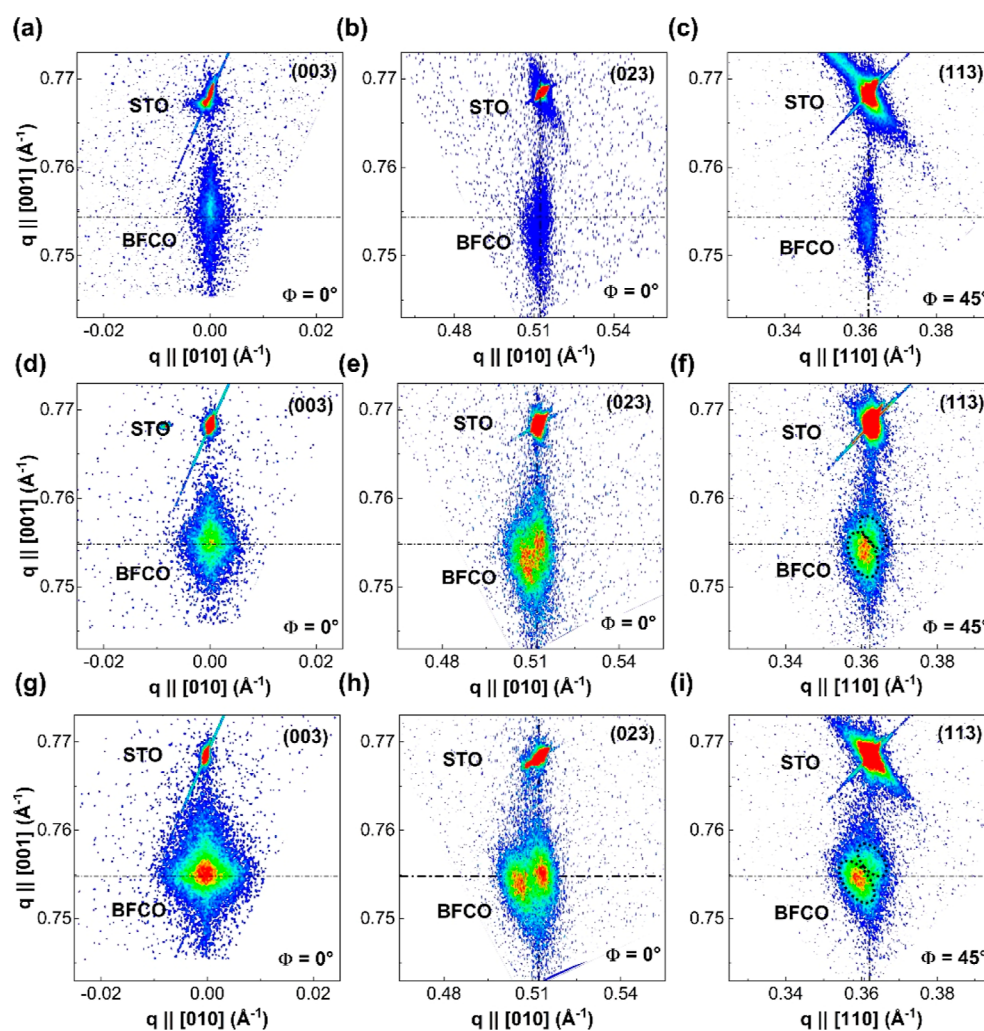
Figure 2. XRD reciprocal space maps for (a−c) 30, (d−f) 70, and (g−i) 130 nm BFCO films.

planes.[26,34] Of note, this behavior appears to be thickness-dependent since the titling did not occur for the sample below 100 nm (see Figure 3b−d).

Based on these findings, we conclude that beyond a specific thickness, tilting of the domains comes to play as an additional mechanism to release the epitaxial stress imposed by the substrate partially (see Figure S8). Hereafter, we only focus on the thinnest and thickest samples representing T-like and R-like structures, respectively.

3.2. First-Principles Calculations. Changes in the strain states or in the crystallographic symmetry induce complex interatomic interaction and thus affect the electronic structure of the material.[36] First-principles calculations can assist in gaining an insight into how the observed crystallographic distortion affects the electronic structure when the system transitions from rhombohedral to tetragonal symmetry.

We started our theoretical study by performing a complete structural characterization of BFCO in the bulk system. Starting from different geometries commonly found in similar perovskites (e.g., orthorhombic *Pnma*, tetragonal *P4mn*, and rhombohedral *R3c*), we identified the experimental rhombohedral and tetragonal structures as represented in Figure 4a. Slight distortions in both phases can be assigned to the effect of the chemical disorder of the solid solution. The predicted c/a ratio for tetragonal BFCO (~1.05) is also smaller than

similar perovskites such as $BiFeO_3$ or $BiCoO_3$, where DFT-calculated values can reach close to 1.30.[37,38]

To overcome the size limitations in the DFT calculations, we aimed to reproduce the physics experienced by the film in the experimental study with the computational approach shown in Figure 4b. In this regard, modifying the in-plane lattice parameter can represent the strain level experienced by the BFCO film when the thickness increases. We constrained the a and b lattice parameters to a fixed value called a_{in} and left the OP lattice parameter c unconstrained and free to relax. The in-plane lattice parameter a_{in} was then subsequently increased from 3.88 Å, to reproduce the thinnest film, to 3.98 Å, which represents a thick-enough film that shares physical properties with the R-like BFCO film. The bandgap was calculated for both phases at different in-plane lattice parameters (Figure 4c). We found that the T-like phase has a slightly smaller bandgap than the R-like one. Moreover, we could discard any critical roles of the lattice strain on the narrowing of the bandgap since the R-like phase has a larger gap than the T-like phase for all investigated in-plane lattice parameters, see Figure 4c. Therefore, the bandgap variation can be assigned almost entirely to structural differences between the T-like and R-like phases.

The partial density of states (pDOS) of both structures, presented in Figure 4d, revealed small but critical differences
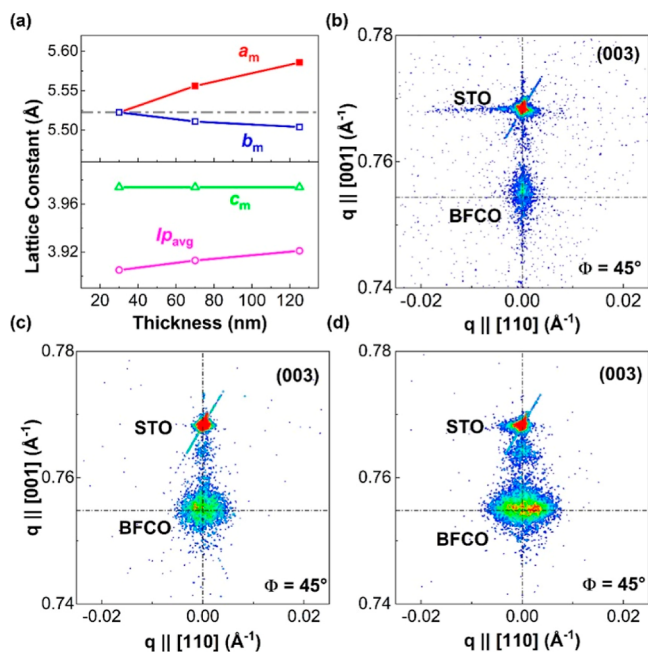
Figure 3. (a) Thickness-Dependent lattice constant (IP_{avg} represents the average in-plane constant in pseudocubic notation). Symmetric (003) RSM plot recorded along [110] for (b) 30, (c) 70, and (d) 130 nm films.

that explain the nature of the BFCO bandgap modulation. In both structures, the conduction band minimum (CBM) is dominated by Fe 3d empty states. Below the Fermi level, oxygen 2p states dominate the valence band with intermixing of the Cr 3d state at the top edge, which is more pronounced in the T-like structure. Like the parental BFO, the occupied Fe d states appear at very low energy, far from the VBM. Hence, the Cr d states at the top of the valence band are responsible for narrowing the bandgap in BFCO compared to BFO.[39] When projected on the individual d-orbitals (Figure S9), the pDOS also confirmed the presence of Fe^{3+} and Cr^{3+} species in both structures, consistent with the representative XPS surface scans as shown in Figure S10. For both R- and T-like structures, the Cr atoms conserve the stable octahedral electron configuration $t_{2g}^3 e_g^0$. In contrast, we notice that the Fe ions transition from an electron configuration compatible with a square-based pyramid coordination in the tetragonal phase ($b_{2g}^1 e_g^2 a_{1g}^1 b_{1g}^1$) to an electron configuration compatible with an octahedral coordination in the rhombohedral system ($t_{2g}^3 e_g^2$). This further splitting of the 3d orbitals in the tetragonal structure is understood to bring the CBM toward the Fermi level and hence narrows the bandgap.[40]

Comparing the electronic structure of different crystallographic symmetries, we note that the band structure of T-like BFCO slightly differs—specifically at the top of the valence band—from that of the R-like structure. For the latter, the
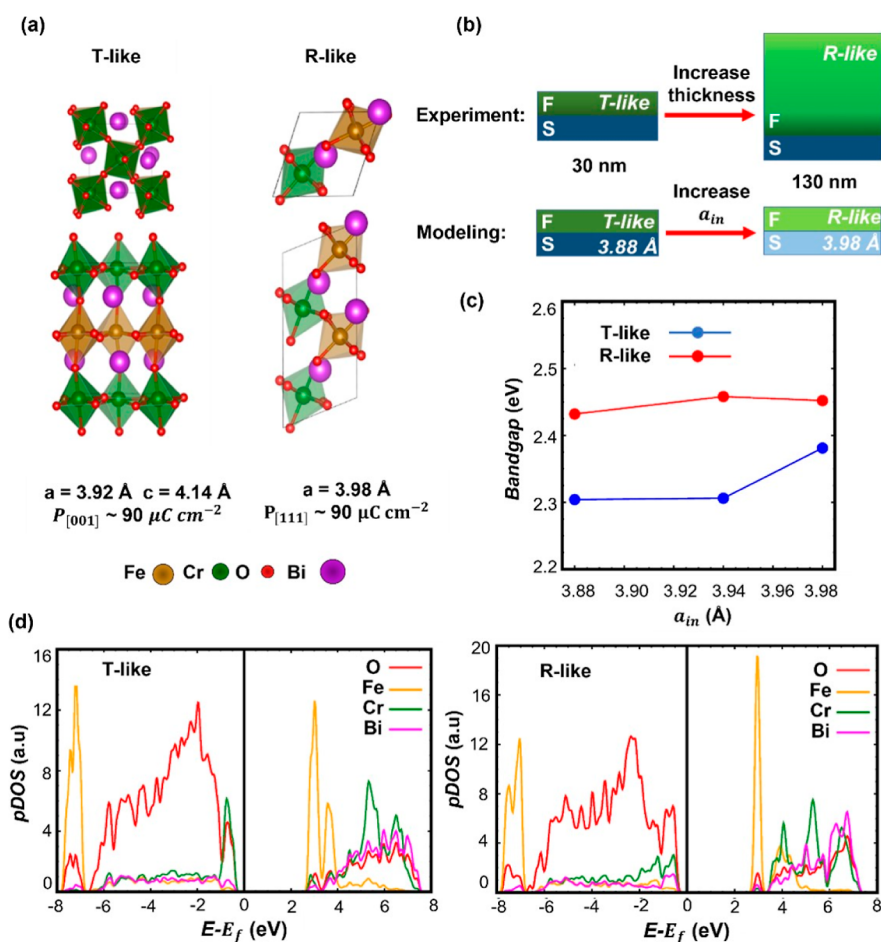

Figure 4. (a) Crystal structure of BFCO; note that the lattice constant is optimized within DFT calculation. (b) Schematic diagram showing the modeling process (S and F represent the substrate and film, respectively). (c) Predicted bandgap modulation. (d) Electronic density of states for two structural variants.

lowest energy charge transfer (CT) is between the unoccupied Fe states and the hybridized oxygen orbitals with cations, while a Mott−Hubbard transition between Cr and Fe can be envisaged for the former in addition to the CT mentioned above. A similar electronic structure has also been reported for the Cr-related oxides previously.[41] Having established both the electronic and crystallographic structure of the BFCO films, we now investigate the optical properties of the BFCO/SRO/STO heterostructure.

3.3. Optical Response. To ascertain the bandgap reduction deduced from DFT results, spectroscopic ellipsometry was employed to extract the optical dispersion law of the films. Figure 5a shows the optical absorption coefficient,
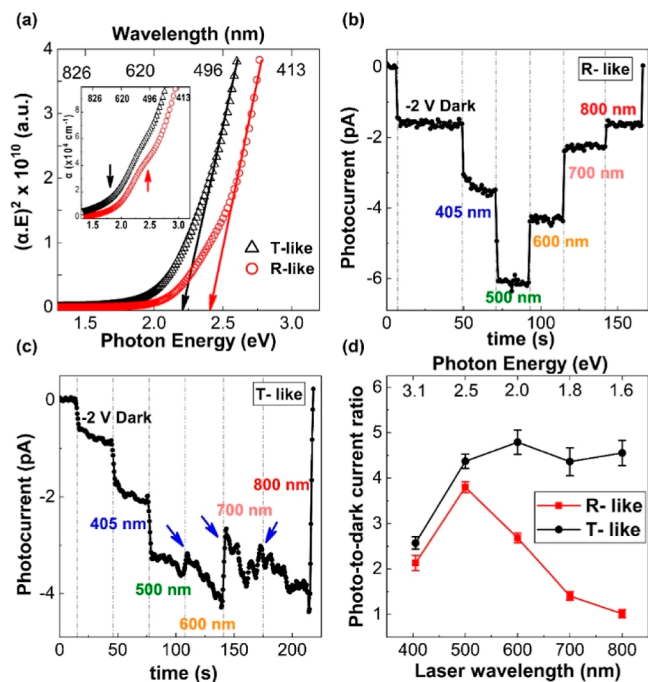

Figure 5. (a) $(\alpha \cdot E)^2$ plot as a function of photon energy for two structural variants (the inset shows the UV−vis absorption spectrum). (b,c) Wavelength-resolved photocurrent for R-like and T-like structures, respectively. (d) Photo-to-dark current ratio of both samples at different laser wavelengths.

together with the Tauc plots of the R-like and T-like films in the range of 1.4−3.2 eV (more details given in Supporting Information Section 9). Despite the complexities associated with the bandgap estimation in such perovskite oxide due to strongly correlated d electrons, the experimental result is consistent with the results of our DFT calculations. The Tauc plots reveal that the direct bandgap for T-like BFCO is reduced by about 150 meV. On a similar note, larger octahedral tilting has promoted a wider bandgap in the hybrid halide perovskite.[42]

To better understand the optical transition in the BFCO thin film, we have acquired the wavelength-resolved photocurrent using the c-AFM setup as described in Methods section (Figure 5b,c). The spectral photocurrent measurement reveals that the absorption onset is below the fundamental direct gap for both structures. Transition metal oxides, in contrast to conventional semiconductors, do not exhibit a sharp absorption edge. Thus, an accurate estimation of E_g from experimental data, e.g., ellipsometry or UV−vis spectrometry,

is not free from ambiguity.[43] The significant finding in Figure 5b,c is that the absorption threshold is red-shifted for the T-like sample, implying that the photon energies of ~1.6 eV (800 nm) can be absorbed. Figure 5d unambiguously distinguishes the T-like photoresponse since, in contrast to the R-like sample, the photo-to-dark current ratio of the T-like structure is greater than unity at wavelengths larger than 700 nm. The red shift of the absorption threshold can be correlated with the higher crystallographic symmetry of the T-like structure, which tunes the d−d CT. Note that the photoresponse of the T-like structure might seem to be larger in magnitude for the photon energies below 2 eV. Upon closer inspection, it appears that it initially decreases by increasing the wavelength (see the blue arrows in Figure 5c), and it then tends to increase as a function of time. The time-dependent photoresponse observed in the T-like structure can be associated with the photoinduced ionic conductivity since such time dependency was not detected in the dark current measurement.[44]

Furthermore, both structures demonstrate a photocurrent maximum at the laser wavelengths close to their estimated direct bandgap. Time-dependent photoresponse at different laser wavelengths was also measured one at a time (Figure S12), ensuring that modulation of photon energy is the main contributor to the observed result. One could also find that photocurrent surprisingly decreases for the above-bandgap photon energies. This observation can be explained by the surface recombination effect, implying that although more carriers are excited at the lower illumination wavelengths, these photoexcited carriers recombine rapidly via surface states and lead to a smaller measurable photocurrent.[45] Of note, the laser intensity used herein, as shown in Figure S13, changes as a function of the wavelength, which can provide further explanation for the lower current under UV illumination.

It is tempting to assign the absorption onset below the fundamental bandgap with CT instabilities associated with self-trapping of excitons.[43,46] However, the energy difference is not reasonable for the excitonic effect. Moreover, defects such as oxygen vacancies have been reported to create in-gap states below the conduction band, resulting in sub-bandgap optical absorption.[47] Nevertheless, since both samples were grown under the same deposition conditions (i.e., oxygen partial pressure and laser fluence) and given the spectral photocurrent measurement demonstrates dependency on the crystallographic symmetry, we propose that the shift of absorption onset is linked to the d−d CT, which can be tuned by adopting a higher symmetry phase.

A closer look at the absorption coefficient extracted for the BFCO films (inset of Figure 5a) shows a clear peak structure around 2.4 eV along with less-pronounced features below 2 eV, which can only be seen once the absorption spectra are deconvoluted. Note that nuances in the spectral features can be disregarded when employing parameterized functions, for example, ellipsometry data analysis, in agreement with the fact that the absorption values vary significantly within the photon energies of 1−6 eV in the BFO-based compounds.[48] These results indicate that the optical transition in the BFCO originates from the complex CTs between O → Fe, O → Cr, Cr → Fe, and Cr → Cr within the visible range. The lowest energy excitation is associated with the d−d CT between metal, e.g., from the occupied Cr 3d t_{2g} state to the unoccupied Fe (or Cr) 3d t_{2g}. Such transition has been previously reported to be separated into sub-bands peaking at ~1.8 and 2.4 eV,[49] in excellent agreement with our results. The analogous

$LaFe_{1-x}Cr_xO_3$ perovskite system also presented an absorption peak located at ~2.4 eV photon energy.[50] Although triggered by changing the laser repetition rate during the film growth, a similar feature in the optical absorption of BFCO film was observed earlier.[14]

3.4. Photoferroelectric Response. To confirm the presence of persistent ferroelectricity in both T-like and R-like BFCO films, we performed domain switching upon application of an external electric field during the PFM measurement. Figure 6a,c shows a clear indication of
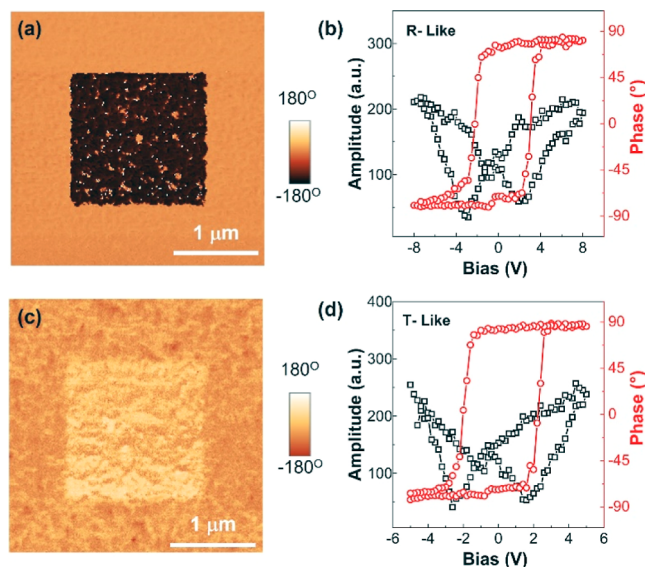
Figure 6. (a,c) Domain switching phase image by writing DC bias (b,d) PFM phase and amplitude hysteresis loop of R-like and T-like BFCO films, respectively.

ferroelectric switching where ferroelectric domains are switched in the inner 1.5×1.5 μm^2 box by applying +8 V from the AFM tip. The T-like BFCO films also exhibit similar domain switching under an external bias (+5 V). Both structural variants display a square-like PFM phase loop and a well-defined butterfly amplitude loop, confirming similar ferroelectric characteristics with a 180° phase change at the coercive voltage (Figure 6b,d).

Moreover, using KPFM, the photoferroelectric response of the BFCO heterostructures was examined. As shown in Figure 7, the variation in the surface potential of the R-like film was measured in the dark and under UV illumination (405 nm). Here, the photoexcited carriers are dissociated due to the built-in field in the BFCO film, leading to a surface potential difference that represents the local spatial photovoltage.[51] The photoinduced surface potential is more evident in the outer region (upward polarization), as shown in Figure 7b, implying the separation of photoexcited carriers and the non-trivial impact of the polarization direction. Figure 7c,d presents the c-AFM images under a bias of −2 V, where a clear contrast between the upward and downward polarization state is evident because the conductivity of the former region is clearly enhanced. Furthermore, the current mapping under UV illumination reveals that light absorption (photon energy of 3 eV) yields mobile carriers contributing to a measurable photocurrent. Of note, the upward polarization (the outer region) appears to allow more photoinduced charge transport
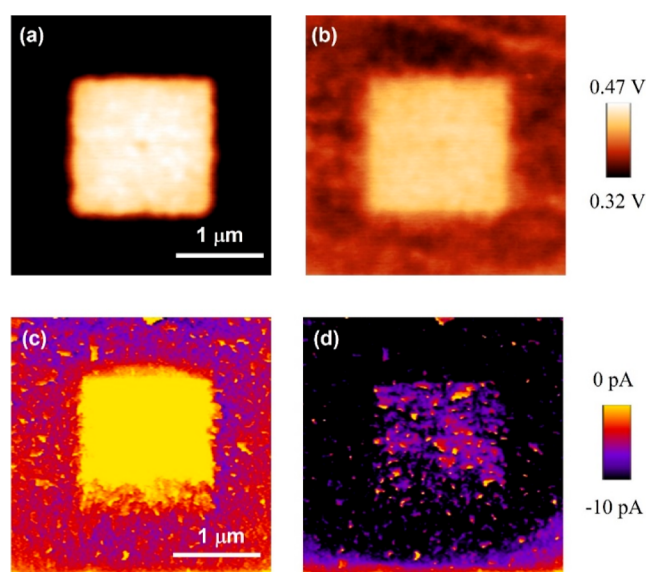
Figure 7. KPFM image of the R-like BFCO film (a) in the dark and (b) under UV illumination (405 nm). c-AFM mapping of the R-like BFCO film (c) in the dark and (d) under UV illumination (405 nm).

since a significant contrast is discernible, suggesting a rectifying behavior.

Note that a severe polarization back-switching to the initial state was observed in the thinner sample, which may arise from the incomplete screening at the ferroelectric/electrode interface (depolarization field),[52] non-switchable interfacial layers,[53] defect dipoles,[54] and the built-in electric field near the ferroelectric/electrode interface.[55] Therefore, to probe the photoelectric response of the T-like BFCO film, as shown in Figure S14, the bottom half of the image was recorded in the dark, while the top half represents the measurement during exposure to the laser source. Figure S14d demonstrates that photoexcited carriers are also generated upon UV light illumination in the T-like BFCO films, contributing to a sizable photocurrent similar to the R-like sample.

To summarize this section, we have demonstrated that despite the bandgap reduction in the T-like BFCO film, both structures present switchable ferroelectric domains along with a noticeable change in the surface potential and photocurrent in the upward polarization regions, suggesting that the photoferroelectric effect occurs under UV illumination.

4. CONCLUSIONS

In summary, we have investigated the thickness-dependent crystallographic evolution of the epitaxial BFCO thin films on SRO-buffered (001) STO substrates. In-depth X-ray reciprocal space mapping provides an insight into the complex strain relaxation mechanisms occurring in these BFCO films, which transition to a lower symmetry phase coupled with the tilt of domains with increasing the film thickness. The present study demonstrates a practical strategy to tune the optical and electronic properties of the BFCO thin films through such a structural phase transition. Using first-principles calculations and spectroscopic ellipsometry, we identified a mechanism to tune the BFCO bandgap, which is likely to be generalized to other oxide perovskites. The T-like BFCO film exhibits a narrower bandgap, and its absorption onset appears about 150 meV lower than in the R-like phase, as confirmed by wavelength-resolved photoresponse measurements. The en-

hanced CT in the T-like structure also shows the potential use of Mott multiferroic BFCO in emerging all-oxide optoelectronic devices. We hope that our results provide the impetus for further research to solve the puzzling relationship between structural and optoelectronic properties in bismuth-based perovskites. This work presents a promising application of ferroelectric oxides in emerging ultrathin PV technologies, where the optical properties of the photoactive layer can be tailored through a structural phase transition. It is worth incorporating thin BFCO films in the multilayered structures for future studies, exploring potential routes to achieve a high-performing and cost-effective multijunction.

ASSOCIATED CONTENT

Ⓢ Supporting Information

The Supporting Information is available free of charge at https://pubs.acs.org/doi/10.1021/acs.jpcc.2c04297.

> AFM images, rocking curve, critical thickness and inhomogeneous strain calculation, projected density of states on individual d-orbitals, XPS spectra, ellipsometry fitted data, time-dependent photoresponse, and comparison of photoelectric response for the samples (PDF)

AUTHOR INFORMATION

Corresponding Author

Danyang Wang — *School of Materials Science and Engineering, The University of New South Wales, Sydney, New South Wales 2052, Australia;* ⓞ orcid.org/0000-0002-7883-8001; Email: dy.wang@unsw.edu.au

Authors

Mohammad Moein Seyfouri — *School of Materials Science and Engineering, The University of New South Wales, Sydney, New South Wales 2052, Australia*

Dawei Zhang — *School of Materials Science and Engineering, The University of New South Wales, Sydney, New South Wales 2052, Australia*

César Menéndez — *School of Chemistry, The University of Sydney, Sydney, New South Wales 2006, Australia*

Daniel Sando — *School of Materials Science and Engineering and ARC Centre of Excellence in Future Low-Energy Electronics Technologies (FLEET), The University of New South Wales, Sydney, New South Wales 2052, Australia; Solid State and Elemental Analysis Unit, Mark Wainwright Analytical Centre, The University of New South Wales, Sydney, New South Wales 2052, Australia;* ⓞ orcid.org/0000-0002-8626-6912

Qi Zhang — *School of Materials Science and Engineering, The University of New South Wales, Sydney, New South Wales 2052, Australia;* ⓞ orcid.org/0000-0003-1940-8471

Claudio Cazorla — *Department de Física, Universitat Politècnica de Catalunya, Barcelona 08034, Spain;* ⓞ orcid.org/0000-0002-6501-4513

Jan Seidel — *School of Materials Science and Engineering and ARC Centre of Excellence in Future Low-Energy Electronics Technologies (FLEET), The University of New South Wales, Sydney, New South Wales 2052, Australia;* ⓞ orcid.org/0000-0003-2814-3241

Complete contact information is available at:
https://pubs.acs.org/10.1021/acs.jpcc.2c04297

Notes

The authors declare no competing financial interest.

REFERENCES

(1) Guo, R.; You, L.; Zhou, Y.; Shiuh Lim, Z. S.; Zou, X.; Chen, L.; Ramesh, R.; Wang, J. Non-volatile memory based on the ferroelectric photovoltaic effect. *Nat. Commun.* **2013**, *4*, 1990.

(2) Rubio-Marcos, F.; Ochoa, D. A.; Del Campo, A.; García, M. A.; Castro, G. R.; Fernández, J. F.; García, J. E. Reversible Optical Control of Macroscopic Polarization in Ferroelectrics. *Nat. Photonics* **2017**, *12*, 29−32.

(3) Kirchartz, T.; Bisquert, J.; Mora-Sero, I.; Garcia-Belmonte, G. Classification of Solar Cells According to Mechanisms of Charge Separation and Charge Collection. *Phys. Chem. Chem. Phys.* **2015**, *17*, 4007−4014.

(4) Heo, J. H.; Im, S. H.; Noh, J. H.; Mandal, T. N.; Lim, C.-S.; Chang, J. A.; Lee, Y. H.; Kim, H.; Sarkar, A.; Nazeeruddin, M. K.; et al. Efficient Inorganic−Organic Hybrid Heterojunction Solar Cells Containing Perovskite Compound and Polymeric Hole Conductors. *Nat. Photonics* **2013**, *7*, 486−491.

(5) Liu, F.; Wang, W.; Wang, L.; Yang, G. Ferroelectric-Semiconductor Photovoltaics: Non-PN Junction Solar Cells. *Appl. Phys. Lett.* **2014**, *104*, 103907.

(6) Paillard, C.; Bai, X.; Infante, I. C.; Guennou, M.; Geneste, G.; Alexe, M.; Kreisel, J.; Dkhil, B. Photovoltaics with Ferroelectrics: Current Status and Beyond. *Adv. Mater.* **2016**, *28*, 5153−5168.

(7) Yang, S. Y.; Seidel, J.; Byrnes, S. J.; Shafer, P.; Yang, C.-H.; Rossell, M. D.; Yu, P.; Chu, Y.-H.; Scott, J. F.; Ager, J. W.; et al. Above-Bandgap Voltages from Ferroelectric Photovoltaic Devices. *Nat. Nanotechnol.* **2010**, *5*, 143−147.

(8) Sando, D.; Yang, Y.; Paillard, C.; Dkhil, B.; Bellaiche, L.; Nagarajan, V. Epitaxial Ferroelectric Oxide Thin Films for Optical Applications. *Appl. Phys. Rev.* **2018**, *5*, 041108.

(9) Seyfouri, M. M.; Wang, D. Recent Progress in Bismuth Ferrite-Based Thin Films as a Promising Photovoltaic Material. *Crit. Rev. Solid State Mater. Sci.* **2021**, *46*, 83−108.

(10) Vats, G.; Bai, Y.; Zhang, D.; Juuti, J.; Seidel, J.; Vats, G.; Zhang, D.; Seidel, J.; Bai, Y.; Juuti, J. Optical Control of Ferroelectric Domains: Nanoscale Insight into Macroscopic Observations. *Adv. Opt. Mater.* **2019**, *7*, 1800858.

(11) Huang, W.; Harnagea, C.; Benetti, D.; Chaker, M.; Rosei, F.; Nechache, R. Multiferroic Bi_2FeCrO_6 Based p−i−n Heterojunction Photovoltaic Devices. *J. Mater. Chem. A* **2017**, *5*, 10355−10364.

(12) Seyfouri, M. M.; Liu, Q.; Yang, J.; Sun, Y.; Dai, X.; Shi, J.; Tan, X.; Li, S.; Wu, T.; Wang, D. New Insights on the Substantially Reduced Bandgap of Bismuth Layered Perovskite Oxide Thin Films. *J. Mater. Chem. C* **2021**, *9*, 3161−3170.

(13) Chakrabartty, J.; Harnagea, C.; Celikin, M.; Rosei, F.; Nechache, R. Improved Photovoltaic Performance from Inorganic Perovskite Oxide Thin Films with Mixed Crystal Phases. *Nat. Photonics* **2018**, *12*, 271−276.

(14) Nechache, R.; Harnagea, C.; Li, S.; Cardenas, L.; Huang, W.; Chakrabartty, J.; Rosei, F. Bandgap Tuning of Multiferroic Oxide Solar Cells. *Nat. Photonics* **2014**, *9*, 61−67.

(15) Suchomel, M. R.; Thomas, C. I.; Allix, M.; Rosseinsky, M. J.; Fogg, A. M.; Thomas, M. F. High Pressure Bulk Synthesis and Characterization of the Predicted Multiferroic $Bi(Fe_{0.5}Cr_{0.5})O_3$. *Appl. Phys. Lett.* **2007**, *90*, 112909.

(16) Kim, D. H.; Lee, H. N.; Biegalski, M. D.; Christen, H. M. Large Ferroelectric Polarization in Antiferromagnetic $BiFe_{0.5}Cr_{0.5}O_3$ Epitaxial Films. *Appl. Phys. Lett.* **2007**, *91*, 042906.

(17) Eng, H. W.; Barnes, P. W.; Auer, B. M.; Woodward, P. M. Investigations of the Electronic Structure of D0 Transition Metal Oxides Belonging to the Perovskite Family. *J. Solid State Chem.* **2003**, *175*, 94−109.

(18) Sando, D. Strain and Orientation Engineering in ABO_3 Perovskite Oxide Thin Films. *J. Phys.: Condens. Matter* **2022**, *34*, 153001.

(19) Tauc, J. Optical Properties and Electronic Structure of Amorphous Ge and Si. *Mater. Res. Bull.* **1968**, *3*, 37−46.

(20) Perdew, J. P.; Burke, K.; Ernzerhof, M. Generalized Gradient Approximation Made Simple. *Phys. Rev. Lett.* **1996**, *77*, 3865.

(21) Dudarev, S. L.; Botton, G. A.; Savrasov, S. Y.; Humphreys, C. J.; Sutton, A. P. Electron-Energy-Loss Spectra and the Structural Stability of Nickel Oxide: An LSDA U Study. *Phys. Rev. B: Condens. Matter Mater. Phys.* **1998**, *57*, 1505.

(22) Blöchl, P. E. Projector Augmented-Wave Method. *Phys. Rev. B: Condens. Matter Mater. Phys.* **1994**, *50*, 17953.

(23) Gonze, X.; Lee, C. Dynamical Matrices, Born Effective Charges, Dielectric Permittivity Tensors, and Interatomic Force Constants from Density-Functional Perturbation Theory. *Phys. Rev. B: Condens. Matter Mater. Phys.* **1997**, *55*, 10355.

(24) Paier, J.; Marsman, M.; Hummer, K.; Kresse, G.; Gerber, I. C.; Ángyán, J. G. Screened Hybrid Density Functionals Applied to Solids. *J. Chem. Phys.* **2006**, *124*, 154709.

(25) Sando, D.; Carrétéro, C.; Grisolia, M. N.; Barthélémy, A.; Nagarajan, V.; Bibes, M. Revisiting the Optical Band Gap in Epitaxial $BiFeO_3$ Thin Films. *Adv. Opt. Mater.* **2018**, *6*, 1700836.

(26) Sando, D.; Han, M.; Govinden, V.; Paull, O.; Appert, F.; Carrétéro, C.; Fischer, J.; Barthélémy, A.; Bibes, M.; Garcia, V.; et al. Interfacial Strain Gradients Control Nanoscale Domain Morphology in Epitaxial $BiFeO_3$. *Adv. Funct. Mater.* **2020**, *30*, 2000343.

(27) Rastei, M. V.; Gellé, F.; Schmerber, G.; Quattropani, A.; Fix, T.; Dinia, A.; Slaoui, A.; Colis, S. Thickness Dependence and Strain Effects in Ferroelectric Bi_2FeCrO_6 Thin Films. *ACS Appl. Energy Mater.* **2019**, *2*, 8550−8559.

(28) Kim, D. H.; Lee, H. N.; Biegalski, M. D.; Christen, H. M. Effect of Epitaxial Strain on Ferroelectric Polarization in Multiferroic $BiFeO_3$ Films. *Appl. Phys. Lett.* **2008**, *92*, 012911.

(29) Venkatesan, S.; Vlooswijk, A.; Kooi, B. J.; Morelli, A.; Palasantzas, G.; De Hosson, J. T. M.; Noheda, B. Monodomain Strained Ferroelectric $PbTiO_3$ Thin Films: Phase Transition and Critical Thickness Study. *Phys. Rev. B: Condens. Matter Mater. Phys.* **2008**, *78*, 104112.

(30) Schlom, D. G.; Chen, L. Q.; Fennie, C. J.; Gopalan, V.; Muller, D. A.; Pan, X.; Ramesh, R.; Uecker, R. Elastic Strain Engineering of Ferroic Oxides. *MRS Bull.* **2014**, *39*, 118−130.

(31) Chu, M. W.; Szafraniak, I.; Scholz, R.; Harnagea, C.; Hesse, D.; Alexe, M.; Gösele, U. Impact of Misfit Dislocation on the Polarization Instability of Epitaxial Nanostructured Ferroelectric Perovskites. *Nat. Mater.* **2004**, *3*, 87−90.

(32) Sando, D.; Appert, F.; Burns, S. R.; Zhang, Q.; Gallais, Y.; Sacuto, A.; Cazayous, M.; Garcia, V.; Fusil, S.; Carrétéro, C.; et al. Influence of Flexoelectricity on the Spin Cycloid in (110)-Oriented $BiFeO_3$ Films. *Phys. Rev. Mater.* **2019**, *3*, 104404.

(33) Catalan, G.; Noheda, B.; McAneney, J.; Sinnamon, L. J.; Gregg, J. M. Strain Gradients in Epitaxial Ferroelectrics. *Phys. Rev. B: Condens. Matter Mater. Phys.* **2005**, *72*, 020102.

(34) Kan, D.; Takeuchi, I. Effect of Substrate Orientation on Lattice Relaxation of Epitaxial $BiFeO_3$ Thin Films. *J. Appl. Phys.* **2010**, *108*, 014104.

(35) Nechache, R.; Harnagea, C.; Pignolet, A. Multiferroic Properties—Structure Relationships in Epitaxial Bi_2FeCrO_6 Thin Films: Recent Developments. *J. Phys.: Condens. Matter* **2012**, *24*, 096001.

(36) Qiao, L.; Jang, J. H.; Singh, D. J.; Gai, Z.; Xiao, H.; Mehta, A.; Vasudevan, R. K.; Tselev, A.; Feng, Z.; Zhou, H.; et al. Dimensionality Controlled Octahedral Symmetry-Mismatch and Functionalities in Epitaxial $LaCoO_3/SrTiO_3$ Heterostructures. *Nano Lett.* **2015**, *15*, 4677−4684.

(37) Menéndez, C.; Chu, D.; Cazorla, C. Oxygen-Vacancy Induced Magnetic Phase Transitions in Multiferroic Thin Films. *npj Comput. Mater.* **2020**, *6*, 1−9.

(38) Menéndez, C.; Cazorla, C. Giant Thermal Enhancement of the Electric Polarization in Ferrimagnetic $BiFe_{1-x}Co_xO_3$ Solid Solutions near Room Temperature. *Phys. Rev. Lett.* **2020**, *125*, 117601.

(39) Sando, D.; Yang, Y.; Bousquet, E.; Carrétéro, C.; Garcia, V.; Fusil, S.; Dolfi, D.; Barthélémy, A.; Ghosez, P.; Bellaiche, L.; et al. Large Elasto-Optic Effect and Reversible Electrochromism in Multiferroic $BiFeO_3$. *Nat. Commun.* **2016**, *7*, 10718.

(40) Chen, P.; Podraza, N. J.; Xu, X. S.; Melville, A.; Vlahos, E.; Gopalan, V.; Ramesh, R.; Schlom, D. G.; Musfeldt, J. L. Optical Properties of Quasi-Tetragonal $BiFeO_3$ Thin Films. *Appl. Phys. Lett.* **2010**, *96*, 131907.

(41) Moore, E. A. First-Principles Study of the Mixed Oxide α-$FeCrO_3$. *Phys. Rev. B: Condens. Matter Mater. Phys.* **2007**, *76*, 195107.

(42) Amat, A.; Mosconi, E.; Ronca, E.; Quarti, C.; Umari, P.; Nazeeruddin, M. K.; Grätzel, M.; De Angelis, F. Cation-Induced Band-Gap Tuning in Organohalide Perovskites: Interplay of Spin−Orbit Coupling and Octahedra Tilting. *Nano Lett.* **2014**, *14*, 3608−3616.

(43) Pisarev, R. V.; Moskvin, A. S.; Kalashnikova, A. M.; Rasing, T. Charge Transfer Transitions in Multiferroic $BiFeO_3$ and Related Ferrite Insulators. *Phys. Rev. B: Condens. Matter Mater. Phys.* **2009**, *79*, 235128.

(44) Zhang, D.; Luo, Z.-D.; Yao, Y.; Schoenherr, P.; Sha, C.; Pan, Y.; Sharma, P.; Alexe, M.; Seidel, J. Anisotropic Ion Migration and Electronic Conduction in van Der Waals Ferroelectric $CuInP_2S_6$. *Nano Lett.* **2021**, *21*, 995−1002.

(45) Bao, X. J.; Schlesinger, T. E.; James, R. B. Electrical Properties of Mercuric Iodide. *Semicond. Semimetals* **1995**, *43*, 111−168.

(46) Schmidt, D.; You, L.; Chi, X.; Wang, J.; Rusydi, A. Anisotropic Optical Properties of Rhombohedral and Tetragonal Thin Film $BiFeO_3$ Phases. *Phys. Rev. B: Condens. Matter Mater. Phys.* **2015**, *92*, 075310.

(47) Basu, S. R.; Martin, L. W.; Chu, Y. H.; Gajek, M.; Ramesh, R.; Rai, R. C.; Xu, X.; Musfeldt, J. L. Photoconductivity in $BiFeO_3$ Thin Films. *Appl. Phys. Lett.* **2008**, *92*, 091905.

(48) Xu, X. S.; Brinzari, T. V.; Lee, S.; Chu, Y. H.; Martin, L. W.; Kumar, A.; McGill, S.; Rai, R. C.; Ramesh, R.; Gopalan, V.; et al. Optical Properties and Magnetochromism in Multiferroic $BiFeO_3$. *Phys. Rev. B: Condens. Matter Mater. Phys.* **2009**, *79*, 134425.

(49) Chamberlin, S. E.; Wang, Y.; Lopata, K.; Kaspar, T. C.; Cohn, A. W.; Gamelin, D. R.; Govind, N.; Sushko, P. V.; Chambers, S. A. Optical Absorption and Spectral Photoconductivity in α-$(Fe_{1−x}Cr_x)_2O_3$ Solid-Solution Thin Films. *J. Phys.: Condens. Matter* **2013**, *25*, 392002.

(50) Andreasson, J.; Holmlund, J.; Knee, C. S.; Käll, M.; Börjesson, L.; Naler, S.; Bäckström, J.; Rübhausen, M.; Azad, A. K.; Eriksson, S. G. Franck-Condon Higher Order Lattice Excitations in the $LaFe_{1-x}Cr_xO_3$ (X=0, 0.1, 0.5, 0.9, 1.0) Perovskites Due to Fe-Cr Charge Transfer Effects. *Phys. Rev. B: Condens. Matter Mater. Phys.* **2007**, *75*, 104302.

(51) Yan, F.; Chen, G.; Lu, L.; Spanier, J. E. Dynamics of Photogenerated Surface Charge on $BiFeO_3$ Films. *ACS Nano* **2012**, *6*, 2353−2360.

(52) Tian, J.; Tan, Z.; Fan, Z.; Zheng, D.; Wang, Y.; Chen, Z.; Sun, F.; Chen, D.; Qin, M.; Zeng, M.; et al. Depolarization-Field-Induced Retention Loss in Ferroelectric Diodes. *Phys. Rev. Appl.* **2019**, *11*, 024058.

(53) Han, M.-G.; Marshall, M. S. J.; Wu, L.; Schofield, M. A.; Aoki, T.; Twesten, R.; Hoffman, J.; Walker, F. J.; Ahn, C. H.; Zhu, Y. Interface-Induced Nonswitchable Domains in Ferroelectric Thin Films. *Nat. Commun.* **2014**, *5*, 1−9.

(54) Arce-Gamboa, J. R.; Guzmán-Verri, G. G. Random Electric Field Instabilities of Relaxor Ferroelectrics. *npj Quantum Mater.* **2017**, *2*, 1−7.

(55) Yu, P.; Luo, W.; Yi, D.; Zhang, J. X.; Rossell, M. D.; Yang, C. H.; You, L.; Singh-Bhalla, G.; Yang, S. Y.; He, Q.; et al. Interface Control of Bulk Ferroelectric Polarization. *Proc. Natl. Acad. Sci. U.S.A.* **2012**, *109*, 9710−9715.

📖 **Recommended by ACS**

Deterministic Influence of Substrate-Induced Oxygen Vacancy Diffusion on Bi_2WO_6 Thin Film Growth

Saikat Das, Yusuke Kozuka, *et al.*

DECEMBER 22, 2020
CRYSTAL GROWTH & DESIGN   READ 🗗

Transition-Metal Substitution-Induced Lattice Strain and Electrical Polarity Reversal in Monolayer WS_2

Peng Zhang, Yongji Gong, *et al.*

APRIL 02, 2020
ACS APPLIED MATERIALS & INTERFACES   READ 🗗

Strain Effects on the Growth of $La_{0.7}Sr_{0.3}MnO_3$ (LSMO)–NiO Nanocomposite Thin Films via Substrate Control

Bethany X. Rutherford, Haiyan Wang, *et al.*

SEPTEMBER 08, 2020
ACS OMEGA   READ 🗗

Bi_2Se_3 Nanolayer Growth on 2D Printed Graphene

Irina V. Antonova, Oleg E. Tereshchenko, *et al.*

AUGUST 17, 2022
CRYSTAL GROWTH & DESIGN   READ 🗗

Get More Suggestions >